

Neural-Network-based NLOS Identification in Angular Domain at 60-GHz

Pengfei Lyu, Aziz Benlarbi-Delaï, Zhuoxiang Ren, *senior member, IEEE*,
and Julien Sarrazin, *senior member, IEEE*

Abstract—This paper introduces an identification method that determines whether a millimeter-wave wireless transmission using directional antennas is being established over a line-of-sight (LOS) or a non-line-of-sight (NLOS) cluster for indoor localization applications. The proposed technique utilizes the channel power angular spectrum that is readily available from a beam training process. In particular, the behavior of five different channel metrics, namely the spatial-domain, time-domain, and frequency-domain channel kurtosis, the mean excess delay, and the RMS delay spread, is analyzed using maximum likelihood ratio and artificial neural network. A noticeable difference between LOS and NLOS clusters is observed and assessed for identification. Hypothesis testing shows errors as low as 0.01-0.02 in simulation and 0.04-0.07 in measurements at 60 GHz.

Index Terms—NLOS identification, millimeter wave, 60 GHz, artificial neural network, indoor localization, beam training.

I. INTRODUCTION

Outdoor wireless localization such as Global Positioning System (GPS) experiences a great success due to its large-scale application. With the booming of the Internet-of-things (IoT), indoor wireless positioning applications are found in many fields such as healthcare, industrial automation, and smart environment [1]. Localization strategies based on existing wireless communication technologies take advantage of saving infrastructure costs. Thanks to their wide bandwidth, millimeter-wave (mm-wave) communications appear as a promising candidate for accurate indoor wireless localization. Operation at mm-wave is included in 5G standard. 3GPP release 15 [2] has defined the use of bandwidth in the 24.25-40 GHz range while release 17 [3] is currently considering frequencies in the 52.6-71 GHz spectrum, including the 60 GHz license-free band. The 60 GHz band is also used in IEEE 802.11ad [4] and IEEE 802.11ay [5] standards for indoor communications based on channel study [6]. In these standards, the total bandwidth at 60 GHz is 8.64 GHz [7], which can provide high positioning accuracy.

Manuscript received August 01, 2020. This work was supported in part by National Key R&D Program of China under Grant 2017YFB020350, National Science Foundation of China under Grants 61501454. This work was performed within NOVIS60 project supported by CEFPRA (Indo-French Center for the Promotion of Advanced Research).

Pengfei Lyu is with the Institute of Microelectronics, Chinese Academy of Sciences, 100029 Beijing, China; School of Microelectronics, University of Chinese Academy of Sciences, 100049 Beijing, China; (e-mail: lvpengfei@ime.ac.cn).

Pengfei Lyu, Julien Sarrazin, Aziz Benlarbi-Delaï, and Zhuoxiang Ren are with Sorbonne Université, CNRS, Laboratoire de Génie Electrique et Electronique de Paris, 75252, Paris, France and with Université Paris-Saclay, CentraleSupélec, CNRS, Laboratoire de Génie Electrique et Electronique de Paris, 91192, Gif-sur-Yvette, France (e-mail: julien.sarrazin@sorbonne-universite.fr).

Color versions of one or more of the figures in this communication are available online at <http://ieeexplore.ieee.org>.

Digital Object Identifier 10.1109/TAP.2016.xxx

Unfortunately, the attenuation of millimeter waves by typical scatterers, such as metal and wood objects [8] and human bodies [9-11], is very high so that the direct path is frequently obstructed by outdoor random building [12, 13] or indoor human activity [14, 15]. The probability of mm-wave communications to operate over indirect paths is thus significantly enhanced, which in turn leads to erroneous estimations of localization metrics such as received signal strength, angle of arrival (AOA), time of arrival (TOA) [16-18], and time difference of arrival [19]. Triangulation-based positioning needs a direct path between transmitters (Tx) and receivers (Rx) to be accurate [16, 20].

Since multipath effect in the 3.1-to-10.6-GHz UWB band is rich [21-23], signals that have propagated along different paths sum up at Rx. In that case, two steps are implemented to mitigate the impact of indirect paths on the localization process [24]. First, the receiver identifies if a direct path exists with a given transmitter, i.e., line-of-sight (LOS) scenario, or not, i.e., non-line-of-sight (NLOS) scenario. Second, the receiver uses the signal received from LOS transmitters only to localize itself and tries to mitigate the error caused by indirect paths in the LOS channel. Signal received from NLOS transmitters are completely discarded, due to the absence of correct position information provided by the direct path. LOS and NLOS channels can be discriminated against by the Rician K -factor for instance [25]. It can be estimated by fitting the measured data with Ricean distribution or by a verified second-order standard moment of the received power intensity [26, 27]. Then, NLOS identification makes a statistical decision [28] based on the difference between the parameters in LOS and NLOS channels [21, 23]. In [29], the kurtosis (i.e., fourth-order moment) of the channel impulse response (CIR) amplitude is introduced as an identification metric. Comparing with other channel features, such as mean total energy, maximum power, amplitude or rise time of the first peak, excess delay, and RMS delay spread [30], kurtosis is independent of the Tx-Rx distance, while depending on the nature of transmission: LOS or NLOS. To make use of those metrics in the identification process, common parametric and non-parametric hypothesis testing methods, such as maximum likelihood ratio (MLR) [29], support vector machine (SVM) [30], and artificial neural network (ANN) [31], are typically employed. After NLOS identification, some regression methods such as least square (LS) or maximum likelihood (ML) [32] are used to mitigate the positioning error in NLOS transmissions.

Different from the rich multipath channel at low-frequency band, the mm-wave channel is sparse [33-35], which exhibits new NLOS identification challenges. To enhance the signal coverage affected by serious blockage, beamforming [36, 37], whether fully-digital [38] or hybrid [39, 40], is used to look for path(s) with high signal-to-noise-ratio (SNR) according to, typically, a discrete multi-beam codebook [41]. Identified high-SNR path(s) are used to establish the communication link, which also provides higher degrees of freedom

for outdoor multi-user scenarios. This beam training strategy is already included in IEEE 802.11ad and IEEE 802.11ay [7, 42, 43] and is attracting more attention in recent years to accelerate it [44, 45]. Unfortunately, while current beam training finds high-SNR links for communication, it is not meant for identifying its nature (i.e., LOS or NLOS), as required for localization. This shortcoming is addressed in this paper.

Although many studies report on indoor [46-48] and outdoor [49-52] localization based on mm-wave 5G system, only a few works [53-56] are dealing with NLOS identification at mm-wave frequencies. To maintain a low-complexity system, the work in [53, 54] uses a simple energy detector to mitigate NLOS components in TOA estimations. However, its robustness to various environments has not been validated with measurements. The work in [56] assumes multiple base stations communicating with a user. However, the channel model used is obtained with a simplified ray tracing, not accounting for diffuse scattering effects, which is however a significant contribution at mm-wave [57]. The work in [55] is to author's best knowledge the only study based on actual experiments at millimeter wave. Based on 28 GHz measurements with quasi-omnidirectional antennas, it uses similar identification approaches than in UWB and so does not consider the directional behavior of the channel.

The work in this paper aims to perform indoor NLOS identification based on the beam training outcomes. Different from current identifications performed onto CIR in time domain [29-31, 55], this work identifies channel's NLOS clusters in the angular domain. All clusters are first found by an image processing method, i.e., watershed segmentation [58], then each of them is classified as LOS or NLOS. The remainder of the paper is organized as follows. In section II, the principle of spatial NLOS cluster identification is presented, including the different physical features between LOS and NLOS transmission, the metrics to identify, and the methods of identification. The method is implemented in simulation in section III based on the IEEE 802.11ad channel model and results are given and discussed. An experimental setup at 60 GHz is used in section IV to validate the proposed approach. Finally, section V draws conclusions and gives some perspectives of this work.

II. PRINCIPLE OF SPATIAL NLOS IDENTIFICATION

The NLOS identification proposed in this paper is performed by analyzing the behavior of five channel metrics, namely the spatial-domain, time-domain, and frequency-domain channel kurtosis, the mean excess delay, and the RMS delay spread. This analysis is done in the elevation/azimuth angular domain using a clustered power angular spectrum (PAS). The statistical distributions of the LOS and NLOS cluster channel metrics are fitted with some distributions whose parameters allows for discrimination (LOS or NLOS). The general procedure is summarized in Fig 1 and is detailed in the following subsections.

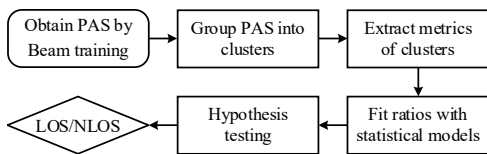


Fig 1 Flow of spatial NLOS identification with beam training

A. Power angular spectrum

The beam training procedure to align Tx and Rx beams consists typically in a channel estimation over the whole angular space in both azimuth (ϕ) and elevation (θ) directions. For instance, the IEEE 802.11ad

standard [7] introduces a beamforming protocol in which the Rx beam sweeps over the whole angular space, while the Tx antenna pattern is kept quasi-omnidirectional. The Rx antenna sweeps then its beam while the Tx pattern is kept quasi-omnidirectional and the link exhibiting the highest link budget may be used for communication. This beam training is performed according to a fixed codebook, in which the angular sweep is done using approximately equal intervals throughout the entire space. Beside enabling establishing a link, such procedure enables the transmitter and/or the receiver to have the knowledge of the spatial representation of the channel, which we propose to use to perform NLOS identification. The PAS, $P(\theta, \phi)$, is defined as the spatial distribution of the channel total power:

$$P(\theta, \phi) = \int_0^T |g_t(\theta, \phi) g_r(\theta, \phi) h(\tau, \theta, \phi) + n(\tau)|^2 d\tau \quad (1)$$

where $g_t(\theta, \phi)$ and $g_r(\theta, \phi)$ are the antenna gains of the transmitter and receiver respectively, $h(\tau, \theta, \phi)$ is the CIR, $n(\tau)$ is an additive white Gaussian noise (AWGN), and T is the channel duration.

An example of PAS generated with the IEEE 802.11ad conference room scenario [4] is shown in Fig 2 (Rx antenna beamwidth of 1° and step size of 1°). Since the 60 GHz channel is sparse [33], the PAS in Fig 2 is composed with high power clusters and a low power background. The first step is to identify and distinguish the different clusters in the PAS onto which an analysis is carried out in order to determine their nature.

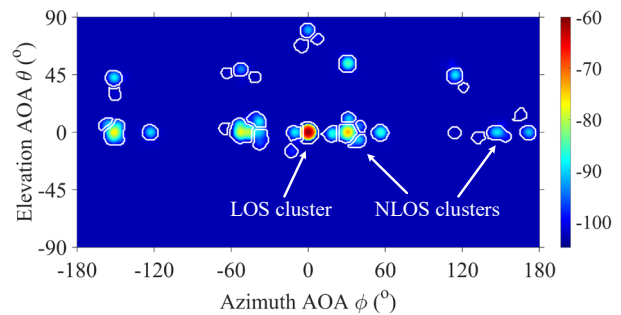


Fig 2 Generation of power angular spectrum obtained with beam training at Rx

B. PAS clustering

In propagation channel modeling, peaks, representing impinging plane waves, are firstly extracted from the channel response and clustering is then performed on a discrete representation of the channel, whether in time or in space [59]. In this paper, the quasi-continuous pixelated PAS 2D map shown in Fig 2 is directly clustered using an image processing-based method described in [58]. The technique identifies the illuminated foreground of the PAS 2D map, i.e., the clusters, from the lower intensity background thanks to several operations including watershed segmentation [58]. In addition to run fast, it preserves the spatial shape of clusters which is of importance for NLOS identification. The resulting contour of identified clusters are shown in Fig 2.

C. Spatial-domain metric: R_p

The LOS cluster, located in the center in Fig 2 ($\theta = \phi = 0^\circ$), exhibits a rotational symmetry (according to the Rx antenna beam shape). However, in NLOS clusters, this symmetry is usually lost. To illustrate this physical phenomenon, a canonical example of Rx beam sweeping simulated with the method of moments is shown in Fig 3. In Fig 3 (a), the received power angular distribution is not affected by scattering objects in the LOS transmission. Thus, the PAS exhibits a shape identical to the Rx radiation pattern. However, in Fig 3 (b), the PAS is randomly deformed by the

distributed scatterers. Even when reflected by smooth reflectors, NLOS clusters are affected as seen in Fig 3 (c).

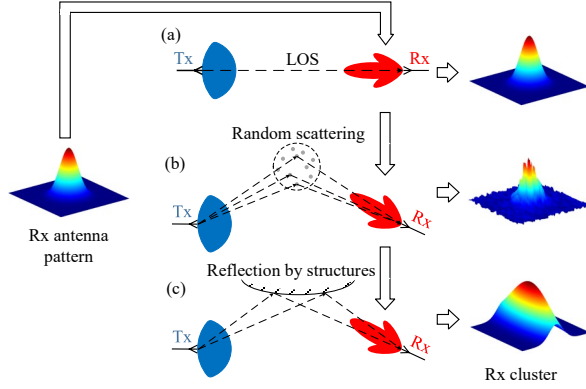


Fig 3 Deformation of clusters due to: (a) LOS transmission; (b) random scattering; (c) mirror-like reflection

The spatial distribution of $P(\theta, \phi)$ is therefore assessed to quantify the difference between LOS and NLOS clusters. By analogy with co-kurtosis of joint probability distribution of two variables, a similar co-kurtosis matrix is introduced to describe the weighted shape of the 2D angular clusters while being independent to the absolute received power:

$$\Sigma_{\rho} = \begin{bmatrix} \rho_{11}(\phi, \phi) & \rho_{12}(\phi, \theta) \\ \rho_{21}(\theta, \phi) & \rho_{22}(\theta, \theta) \end{bmatrix} \quad (2)$$

where the elements ρ_{ij} are the co-kurtosis for azimuth and elevation angles given by:

$$\rho_{11} = \frac{\sum (\phi_i - \bar{\phi}_i)^4 P(\phi_i, \phi_i)}{\sum P(\phi_i, \phi_i)} / \sigma_{11}^2 \quad (3)$$

$$\rho_{12} = \rho_{21} = \frac{\sum (\phi_i - \bar{\phi}_i)^2 (\theta_i - \bar{\theta}_i)^2 P(\phi_i, \theta_i)}{\sum P(\phi_i, \theta_i)} / \sigma_{12}^2 \quad (4)$$

$$\rho_{22} = \frac{\sum (\theta_i - \bar{\theta}_i)^4 P(\theta_i, \theta_i)}{\sum P(\theta_i, \theta_i)} / \sigma_{22}^2 \quad (5)$$

with θ_i and ϕ_i , the azimuth and elevation angle of the i -th element in a given cluster, $\bar{\theta}_i$ and $\bar{\phi}_i$, the mean angles for the given cluster, and σ , the azimuth or elevation standard deviation weighted with power P :

$$\sigma_{11} = \frac{\sum (\phi_i - \bar{\phi}_i)^2 P(\phi_i, \phi_i)}{\sum P(\phi_i, \phi_i)} \quad (6)$$

$$\sigma_{12} = \sigma_{21} = \frac{\sum (\phi_i - \bar{\phi}_i)(\theta_i - \bar{\theta}_i) P(\phi_i, \theta_i)}{\sum P(\phi_i, \theta_i)} \quad (7)$$

$$\sigma_{22} = \frac{\sum (\theta_i - \bar{\theta}_i)^2 P(\theta_i, \theta_i)}{\sum P(\theta_i, \theta_i)} \quad (8)$$

By weighting the shape of the clusters by $P(\theta, \phi)$, the co-kurtosis matrix offers a simple mean to quantify its spatial distribution. As observed earlier, the nature of the propagation influences the symmetry of clusters. The weighted symmetry is a measurable quantity to evaluate the shape of

clusters. By analogy to principal component analysis (PCA) in statistics, the ratio R_P of minimum eigenvalue over maximum eigenvalue of the co-kurtosis matrix (2) can be used to characterize the spatial symmetry of the kurtosis of the different clusters' power,

$$R_P = \frac{\min(\lambda_1, \lambda_2)}{\max(\lambda_1, \lambda_2)} \quad (9)$$

where λ_1 and λ_2 are the eigenvalues with the corresponding eigenvectors \mathbf{v}_1 and \mathbf{v}_2 through decomposition of co-kurtosis matrix (2):

$$\Sigma_{\rho} = [\mathbf{v}_1 \mathbf{v}_2] \begin{bmatrix} \lambda_1 & 0 \\ 0 & \lambda_2 \end{bmatrix} [\mathbf{v}_1 \mathbf{v}_2]^{-1} \quad (10)$$

D. Time-domain metrics: K_t , τ , τ_{RMS}

Besides power, intra-cluster features in time and frequency domain also differ between LOS and NLOS clusters. An example of the power CIR inside clusters is shown in Fig 4 (a)¹. The first peak is much stronger than the other peaks in the LOS situation whereas it is not the case in NLOS where the power is more spread over time. The probability density function (PDF) of the CIR power distribution in Fig 4 (a) is shown in Fig 4 (b). It can be observed that the NLOS PDF is more spread than the LOS.

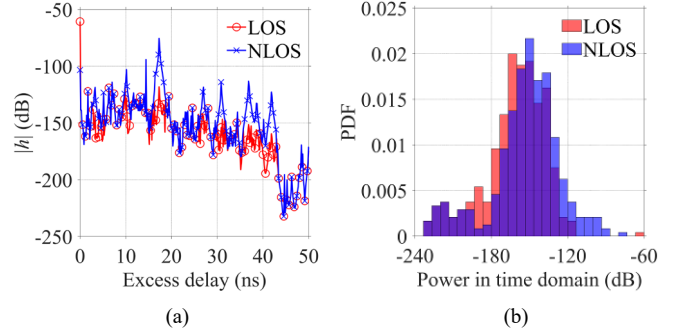


Fig 4 (a) CIR and (b) PDF of CIR inside LOS and NLOS clusters of PAS generated by the IEEE 802.11ad channel model of conference room scenario.

To obtain a metric representative of such effect and being independent to the absolute received power, the kurtosis K_t is used to evaluate the shape of the PDF of the CIR distribution:

$$K_t(\theta, \phi) = \frac{E_{\tau} \left[\left(|h(\tau, \theta, \phi)| - \mu_{|h|} \right)^4 \right]}{E_{\tau} \left[\left(|h(\tau, \theta, \phi)| - \mu_{|h|} \right)^2 \right]^2} \quad (11)$$

where $\mu_{|h|}$ is the mean of CIR over excess delay τ and $E_{\tau}[\cdot]$ is the expectation operator over excess delay τ . This time-domain kurtosis is therefore the second metric used in this paper to perform NLOS identification. The third and fourth metrics are the mean excess delay τ and the RMS delay spread τ_{rms} , calculated as:

$$\bar{\tau}(\theta, \phi) = \frac{\int_0^T \tau |h(\tau, \theta, \phi)|^2 d\tau}{\int_0^T |h(\tau, \theta, \phi)|^2 d\tau} \quad (12)$$

$$\tau_{rms}(\theta, \phi) = \sqrt{\frac{\int_0^T (\tau - \bar{\tau})^2 |h(\tau, \theta, \phi)|^2 d\tau}{\int_0^T |h(\tau, \theta, \phi)|^2 d\tau}} \quad (13)$$

¹ The simulation conditions are detailed in section III-A.

Because of local random scattering experienced by multipath components while reflecting on rough surfaces, NLOS clusters are expected to exhibit larger $\bar{\tau}$ and τ_{rms} values, as typically observed in various channel environments [30].

E. Frequency-domain metric: K_f

In frequency domain, the selective behavior of the channel can be observed in the channel frequency response (CFR) in Fig 5 (a). While the CFR appears almost flat in the LOS case, it exhibits fluctuations in NLOS case. However, excluding the influence of the absolute received power, the difference is less remarkable as illustrated by the CFR PDF² in Fig 5 (b). Nevertheless, LOS and NLOS PDF still exhibit slightly different shapes that are assessed in next sections using the kurtosis of the CFR as the fifth identification metric:

$$K_f(\theta, \phi) = \frac{E_f \left[\left(|H(f, \theta, \phi)| - \mu_{|H|} \right)^4 \right]}{E_f \left[\left(|H(f, \theta, \phi)| - \mu_{|H|} \right)^2 \right]^2} \quad (14)$$

where $\mu_{|H|}$ is the CFR mean and $E_f[\cdot]$ is the expectation operator over frequency.

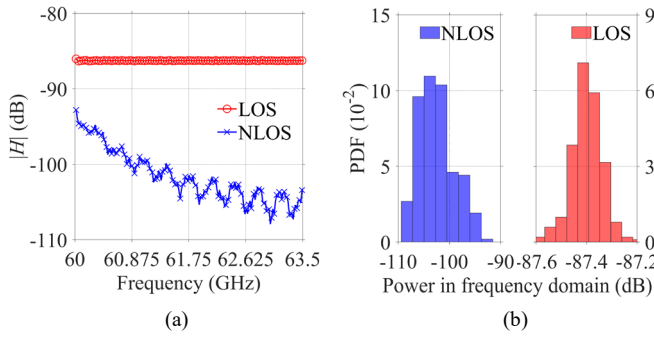


Fig 5 (a) CFR $|H(f)|$ and (b) PDF of CFR inside LOS and NLOS clusters of PAS generated by the IEEE 802.11ad channel model of conference room scenario.

F. Statistical model and decisions

Since clusters are affected by randomly distributed scatterers in an indoor scenario, the metrics associated with LOS clusters (R_P^{los} , K_t^{los} , τ_c^{los} , τ_{rms}^{los} , and K_f^{los}) and NLOS clusters (R_P^{nlos} , K_t^{nlos} , τ_c^{nlos} , τ_{rms}^{nlos} , and K_f^{nlos}) are stochastic variables. Therefore, the identification is a hypothesis testing: a LOS propagation hypothesis is defined as the null hypothesis, H_0 , while the alternative hypothesis, H_1 , is NLOS propagation:

$$\begin{aligned} H_0: & \text{LOS propagation with } R_P^{los}, K_t^{los}, \tau_c^{los}, \tau_{rms}^{los}, \text{ and } K_f^{los} \\ H_1: & \text{NLOS propagation with } R_P^{nlos}, K_t^{nlos}, \tau_c^{nlos}, \tau_{rms}^{nlos}, \text{ and } K_f^{nlos} \end{aligned} \quad (15)$$

Two classifiers are investigated to test the above hypothesis: MLR and ANN. The aim of MLR is to test the probability distribution from which the likelihood with the observations is sampled. The features are modeled by conditional PDFs, $f(m | \theta^{los})$ and $f(m | \theta^{nlos})$ with parameter vectors θ^{los} and θ^{nlos} for LOS and NLOS propagation, respectively. The hypothesis (15) is then written as:

$$\begin{aligned} H_0: & \hat{m}_i \sim f(m_i | \theta_i^{los}) \\ H_1: & \hat{m}_i \sim f(m_i | \theta_i^{nlos}) \end{aligned} \quad (16)$$

where m_i are the i -th observed metrics: R_P , K_t , τ_c , τ_{rms} , or R_f . The PDFs expressions used for all m_i are the same. Specifically, generalized extreme value (GEV) are used for both simulation and measurement, as detailed in next sections. The parameters θ_i of the above PDFs are estimated by fitting a set of training m_i with maximum likelihood estimation. With the estimated parameters, the hypothesis is tested by comparing which likelihood (LOS or NLOS) is larger at an individual testing \hat{m}_i under the trained PDFs. Since the unique difference between the LOS and NLOS PDFs for a given feature \hat{m}_i is the parameter θ_i , the testing becomes the comparison between the likelihood of parameters (θ_i^{los} or θ_i^{nlos}) for a given \hat{m}_i . Therefore, the comparison is achieved by the likelihood ratio of the PDF parameter θ_i at a given testing \hat{m}_i (\hat{R}_P , \hat{K}_t , $\hat{\tau}_c$, $\hat{\tau}_{rms}$, or \hat{K}_f):

$$L(\hat{m}_i) = \frac{\mathcal{L}(\theta_i^{los}; \hat{m}_i)}{\mathcal{L}(\theta_i^{nlos}; \hat{m}_i)} \underset{H_1}{\overset{H_0}{\geq}} 1 \quad (17)$$

where $\mathcal{L}(\theta_i^{los}; \hat{m}_i)$ and $\mathcal{L}(\theta_i^{nlos}; \hat{m}_i)$ are likelihood functions of the statistical parameter θ_i at a given testing \hat{m}_i for LOS and NLOS propagation, respectively. Therefore, the joint likelihood ratio of \hat{R}_P , \hat{K}_t , $\hat{\tau}_c$, $\hat{\tau}_{rms}$, and \hat{K}_f is:

$$L(\hat{R}_P, \hat{K}_t, \hat{\tau}_c, \hat{\tau}_{rms}, \hat{K}_f) = \prod_i \frac{\mathcal{L}(\theta_i^{los}; \hat{m}_i)}{\mathcal{L}(\theta_i^{nlos}; \hat{m}_i)} \underset{H_1}{\overset{H_0}{\geq}} 1 \quad (18)$$

The second investigated method to classify the features is the ANN, here constructed with one input layer, two hidden layers, and one output layer, as shown in Fig 6.

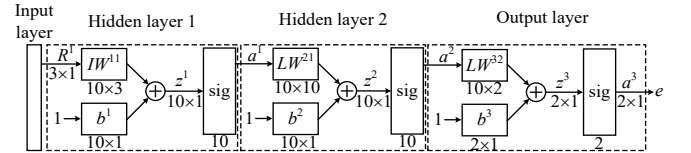


Fig 6 Architecture of the ANN used for NLOS identification

The whole network in Fig 6 can be expressed as:

$$a^3 = \text{sig} \left(LW^{32} \cdot \text{sig} \left(LW^{21} \cdot \text{sig} \left(IW^{11} m^1 + b^1 \right) + b^2 \right) + b^3 \right) \quad (19)$$

The input is the parameter vector $m^1 = [\hat{R}_P, \hat{K}_t, \hat{\tau}_c, \hat{\tau}_{rms}, \hat{K}_f]^T$. There are ten neurons in all hidden layers. The input weighting matrix in the first hidden layer IW^{11} is a 10×3 matrix. LW^{21} in the hidden layer and LW^{32} in the output layer are respectively 10×10 and 10×2 weighting matrices. b^1 , b^2 , and b^3 are the bias vectors in layers 1, 2, and 3, respectively. An activation function maps the input set to an output set. For null hypothesis testing, the output set of the whole network has to be $\{-1, 1\}$, while the output of the linear weighted combination part is a real set. Therefore, the activation of output is a map $\mathbb{R} \rightarrow \{-1, 1\}$. The simplest activation function is a step function. However, the step function introduces a non-derivative singularity at the origin. To avoid this issue, the activation functions in the hidden layers are both nonlinear tangent sigmoid function $\text{sig}(x) = 2 / [1 + \exp(-2x)] - 1$. The curve linearly increases in the range of $[-1, 1]$, while approximately being constant to $+1$ at the top bound and to -1 at the bottom bound. The activation function of the output layer is a

²The simulation conditions to obtain the PDF are detailed in section III-A.

normalization function $sig(x) = \exp(x) / \sum \exp(x)$. It proportionally maps an input vector into a range of [0, 1]. ANN training aims to optimize the weighting matrices and the bias vectors to minimize the error e between the training result a^3 and the marked label y whose values are either 0 (LOS) or 1 (NLOS) using gradient descent:

$$e = (y - a^3)^2 \quad (20)$$

III. SIMULATION RESULTS

A. Simulation conditions

The simulation follows the procedure in Fig 1. The PAS is firstly obtained by beam training using the IEEE 802.11ad channel. The channel is built-in conference scenario where a pair of Tx and Rx are placed on a table at the center of a conference room with an area of $4.3 \text{ m} \times 3 \text{ m} \times 3 \text{ m}$ [4]. The scenario is as per as the beam training strategy: the Tx antenna is omnidirectional, while the directional Rx antenna rotates across the whole angular space. The scanning step is 1° . The beam pattern of the antenna model is a single main lobe with a symmetric Gaussian shape. Similar to the actual antenna used in the measurement in the next section, the half-power beamwidth (HPBW) of the Rx antenna is taken as 5° . A sampling frequency of 7 GHz is used in the IEEE 802.11ad channel model generation. 250 Monte Carlo simulations are performed to obtain enough data for a statistical description of the performance. Among the realizations, 150 of them are used to train PDFs and 100 of them are used for hypothesis testing. The obtained PAS are clustered with the watershed algorithm in [58]. The cluster metrics are calculated according to (10), (11), (12), (13), and (14).

B. Statistical characteristics of metrics

The statistical behavior of co-kurtosis eigenvalue ratio of power R_P , time-domain kurtosis K_t , mean excess delay $\bar{\tau}$, RMS delay spread τ_{rms} , or frequency-domain kurtosis K_f is described with PDF that is fitted with GEV distributions to obtain reference parameters to be used for classification in the next section. The expression of GEV PDF and CDF are respectively given by:

$$f_i(x | \gamma_i, \mu_i, \sigma_i) = \begin{cases} \frac{1}{\sigma_i} \exp \left[- \left(1 + \gamma_i \frac{x - \mu_i}{\sigma_i} \right)^{-1/\gamma_i} \right] \left(1 + \gamma_i \frac{x - \mu_i}{\sigma_i} \right)^{-(1+1/\gamma_i)}, & \gamma_i \neq 0 \\ \frac{1}{\sigma_i} \exp \left[- \exp \left(- \frac{x - \mu_i}{\sigma_i} \right) - \frac{x - \mu_i}{\sigma_i} \right], & \gamma_i = 0 \end{cases} \quad (21)$$

$$F_i(x | \gamma_i, \mu_i, \sigma_i) = \begin{cases} \exp \left[- \left(1 + \gamma_i \frac{x - \mu_i}{\sigma_i} \right)^{-1/\gamma_i} \right], & \gamma_i \neq 0 \\ \exp \left[- \exp \left(- \frac{x - \mu_i}{\sigma_i} \right) \right], & \gamma_i = 0 \end{cases} \quad (22)$$

where $\theta_i = \{\gamma_i, \mu_i, \sigma_i\}$ are the parameters corresponding to the i -th metric used in the likelihood functions in (17) and (18).

Monte Carlo simulations and fitted GEV distributions are given in Fig 7-9 where a fair agreement can be observed. For the spatial eigenvalue ratio of power co-kurtosis matrix \hat{R}_P , it can be qualitatively observed in Fig 7 that the LOS clusters exhibit a large symmetry as the PDFs tend to rapidly grow when the min/max eigenvalue ratios reach 1. In particular, it is observed that 90 % of the min/max eigenvalue ratios in LOS transmission is concentrated in a range from 0.86 to 1. For NLOS clusters, PDFs appear more uniformly distributed and there is no specific

tendency for min/max eigenvalue ratios to be equal to a particular value. This shows that the spatial shape of NLOS cluster metrics is less consistent. The LOS cluster behavior is also observed in the LOS CDF curves, where an exponential-like increase occurs as ratios get close to 1. The wide min/max eigenvalue ratios spread observed in the NLOS PDF is represented by the almost linear behavior of the NLOS CDF curves. These results mean that, as expected, statistically, the channel metric \hat{R}_P behaves similarly in both azimuth and elevation planes in LOS clusters, while it is stochastically affected by the random scattering in NLOS clusters and therefore behave differently in both angular planes. The LOS and NLOS CDF curves are clearly different from each other, and there is only 20% probability that LOS and NLOS PDF overlap which indicates a promising indicator for LOS/NLOS discrimination.

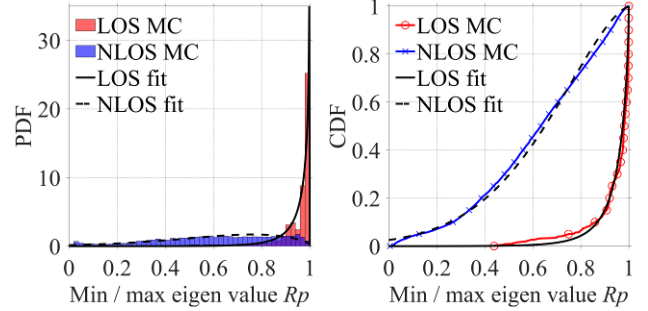


Fig 7 PDF and CDF of simulated co-kurtosis eigenvalue ratios R_P

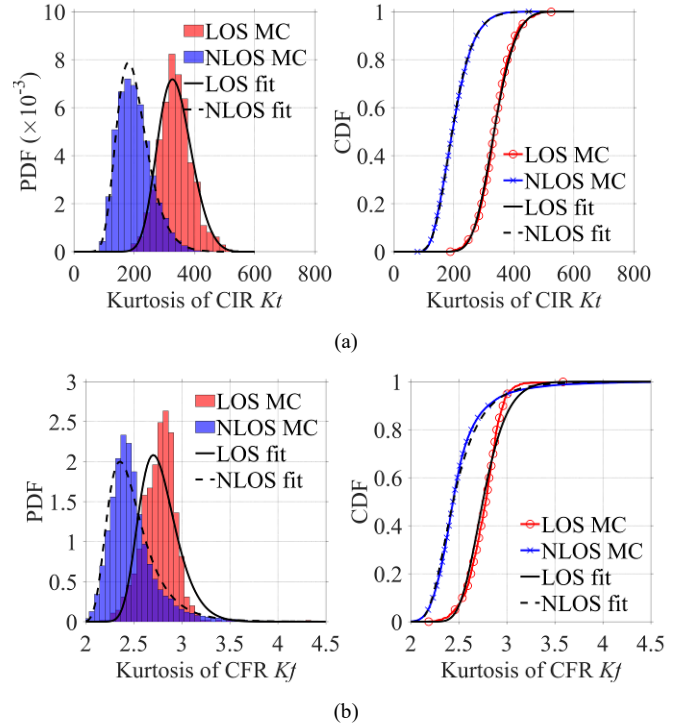


Fig 8 PDF and CDF of simulated (a) time-domain kurtosis K_t and (b) frequency-domain kurtosis K_f

The PDF and CDF of time- and frequency-domain kurtosis, K_t and K_f , are shown in Fig 8. 90% of K_t values in NLOS clusters are lower than 276 as shown in Fig 8 (a), while it is only 12% in LOS clusters. However, LOS and NLOS PDFs exhibit a 35% overlap. So a certain ambiguity can arise for identification, especially in the [200, 400] range. In frequency-domain, 99% of K_f values in NLOS clusters are distributed in the [2.0, 3.7] range, which entirely covers the [2.2 3.1]

range that contains 99% of LOS K_f values as seen in Fig 8 (b). The LOS and NLOS CDF are therefore not too different. The clearer distinction offered by K_t over K_f is consistent with the example of PDFs shown in Fig 4 (b) Fig 5 (b).

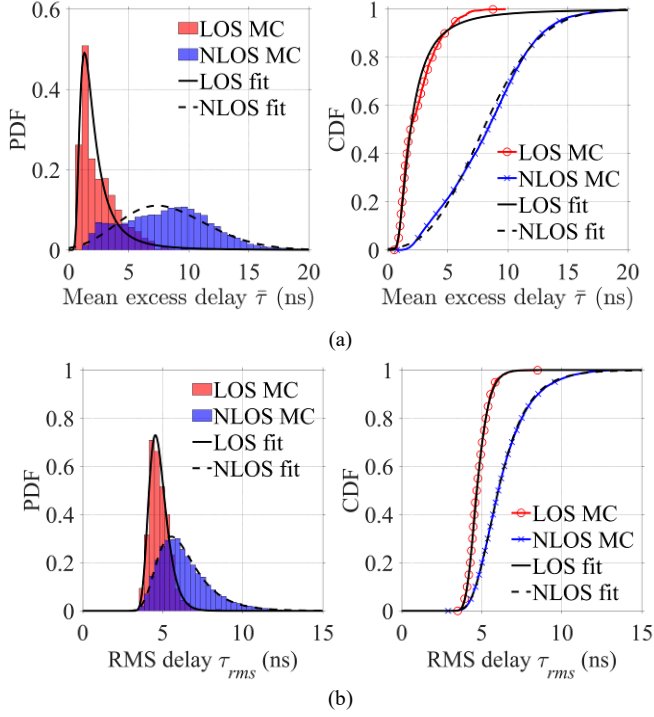


Fig 9 PDF and CDF of simulated (a) mean excess delay $\bar{\tau}$ and (b) RMS delay spread τ_{rms} .

Table 1 Parameters of GEV distribution obtained to fit the CDF

Metrics	Parameters	LOS	NLOS
R_p	γ_p	-1.363	-0.6214
	μ_p	0.9579	0.5588
	σ_p	0.0574	0.2789
	RMSE	0.0808	0.0217
K_t	γ_t	-0.2142	-0.0658
	μ_t	318.9	177.6
	σ_t	53.49	46.93
	RMSE	0.0155	0.0074
K_f	γ_f	-0.0813	0.0806
	μ_f	2.689	2.369
	σ_f	0.1759	0.1848
	RMSE	0.0411	0.0199
$\bar{\tau}$	γ_τ	0.3242	-0.1822
	μ_τ	1.493	6.673
	σ_τ	0.7359	3.388
	RMSE	0.0342	0.0179
τ_{rms}	γ_{rms}	-0.0417	0.0483
	μ_{rms}	4.514	5.590
	σ_{rms}	0.5047	1.195
	RMSE	0.0071	0.0036

The PDF and CDF of mean excess delay $\bar{\tau}$ and RMS delay spread τ_{rms} are shown in Fig 9 (a), where the difference in LOS and NLOS statistical behavior can be observed. 91% of LOS clusters exhibit mean excess delays less than 5 ns whereas only 21% of LOS clusters do so. However, the difference in LOS/NLOS behavior in terms of RMS delay is not so clear as seen in Fig 9 (b). PDFs overlap over a

large area in the range 3.2 ns to 6.7 ns. So, on one hand, the diffusion in NLOS clusters introduces a larger excess delay, while on the other hand, the strong mm-wave attenuation faced by the diffused components does not increase much the RMS delay spread.

The parameters of the GEV distribution and the root mean squared error (RMSE) between fitted and empirical CDF are listed in Table 1. The RMSE of LOS and NLOS CDF is lower than 0.0808 and 0.022 respectively.

C. Performance of NLOS identification

The performance of the classifiers is evaluated with the probability of incorrect decisions for a set of testing data. According to statistical decision theory, for a null hypothesis testing, the error can be classified as two types: type I error (reject the true null hypothesis H_0) and type II error (non-reject the false alternative hypothesis H_1). So according to (15), a type I error is a LOS transmission identified as NLOS and a type II error is an NLOS transmission classified as LOS. The error is evaluated by comparing the type of transmission decided by the classifiers with the actual type of transmission and results are shown in Table 2.

Table 2 Simulated probabilities of error tested for NLOS identification

Methods	Metrics	Type I	Type II
MLR	R_p	0.1060	0.1580
	K_t	0.0820	0.1163
	K_f	0.1140	0.2840
	$\bar{\tau}$	0.1760	0.1398
	τ_{rms}	0.1540	0.3026
	$R_p, K_t, K_f, \bar{\tau}, \tau_{rms}$	0.0980	0.0355
ANN	$[R_p, K_t, K_f, \bar{\tau}, \tau_{rms}]$	0.0235	0.0150

Error results differ with metrics and classification methods. Using metrics individually with MLR, the time-domain kurtosis leads to the lowest type I and II errors. Using all metrics improves results, especially for type II error. ANN performs better for both type I and II errors. Indeed, different from simply comparing the probability with MLR, the relation among the metrics is discovered by ANN and gives more information regarding LOS and NLOS differences. Overall, values appear small enough to consider this approach for NLOS identification.

IV. EXPERIMENTAL VALIDATION

A. Measurement conditions

To validate the proposed approach, experiments are conducted in a laboratory environment. Measurements are performed in a quasi-rectangle room in a microwave wireless facilities lab at Sorbonne University. The size of the room is approximately 10.25 m \times 7.52 m. The distance between the ground and the ceiling is 2.93 m. The floor plane of the measuring environment is illustrated in Fig 10. Measurements are randomly implemented in the zones which are marked as closed circles in the floor plane: direct paths are blocked in green circles and unblocked in red circles. Both Tx and Rx are in the same zone for a given set of experiments with the distance between Tx and Rx ranging from 0.5 to 2.5 meters. A total of 100 PAS samples are measured. Since this represents a relatively small data set (a single PAS measurement lasts about 3.5 hours), bootstrapping method is used to artificially augment it [60]. 30 samples are randomly extracted from the population as a set, while 20 samples are randomly extracted from the rest to construct the testing set. After repeating the training and testing 10 times, the final model and hypothesis testing performance are obtained by averaging results over the 10 training and testing.

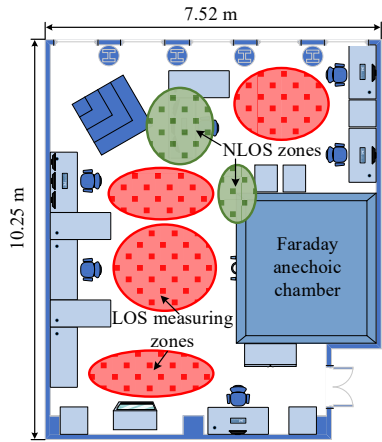


Fig 10 Floor plane of the experiments.

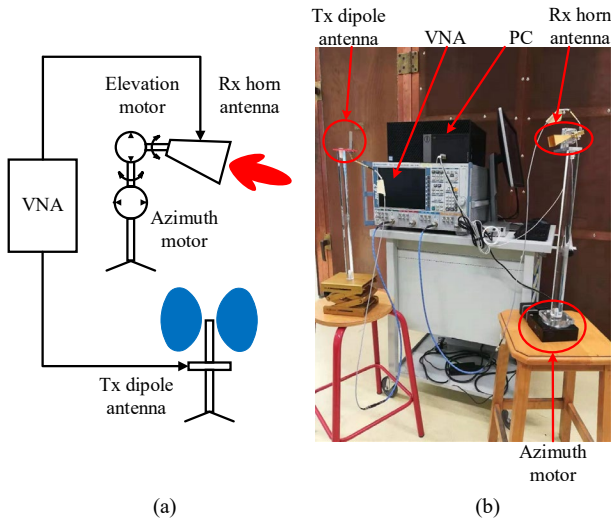


Fig 11 (a) Schematic and (b) photo of the measurement system

Table 3 Parameters of the purposed measurement system

Bandwidth	8.64 GHz
Time resolution	0.12 ns
Frequency resolution	11.5 MHz
Transmit power	4 dBm
Noise level	-100 dBm
Rx beam width (E/H plane)	10.1° / 13.1°
Tx beam width (E/H plane)	360° / 60°
Tx antenna gain	2 dB
Rx antenna gain	24 dB
Sampling range in azimuth	[-180°, 180°]
Sampling range in elevation	[-45°, 90°]
Spatial sampling interval	5°

The measurement configuration set-up aims at emulating a beam training strategy as shown in Fig 11. A vector network analyzer (VNA) is used to measure the propagation channel, between Tx and Rx antennas. Tx antenna is a quasi-omnidirectional dipole antenna with 2 dB gain, while the Rx antenna is a directional horn antenna with about 5° HPBW and 24 dB gain. The beam training is achieved with Rx spatial scanning in vertical and horizontal directions by an azimuth motor and an elevation motor respectively. The sweeping steps are 5° in both directions. The parameters are listed in Table 3.

B. Clustering PAS

An example of measured PAS is shown in Fig 12, along with the identified clusters. The cluster shape is here less accurate than in simulation due to the large angular step size used in measurements because of experimental time constraint and a higher background spatial noise that jeopardizes to some extent the watershed-based segmentation process (see [58] for more discussion about the performance of PAS clustering in experimental conditions). However, the identified clusters cover most of the power of the actual clusters, which are the domains within which the type of propagation is tested.

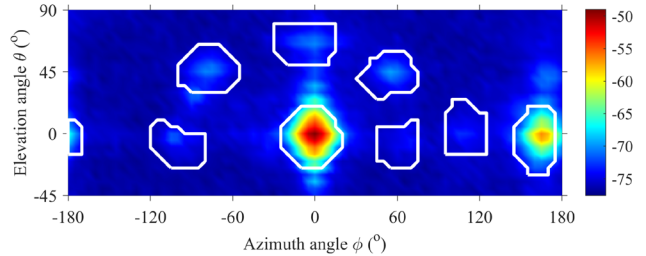


Fig 12 Example of measured PAS in dB with clusters identified by watershed segmentation.

C. Statistical characteristics of metrics

The PDF and CDF of the measured co-kurtosis eigenvalue ratio of power R_p , is shown in Fig 13. The LOS eigenvalue ratio concentrates near 0.7³ while the NLOS eigenvalue ratio is more spread in the 0-1 range. This is consistent with simulation results in Fig 7 and a clear difference between LOS and NLOS behavior can be observed.

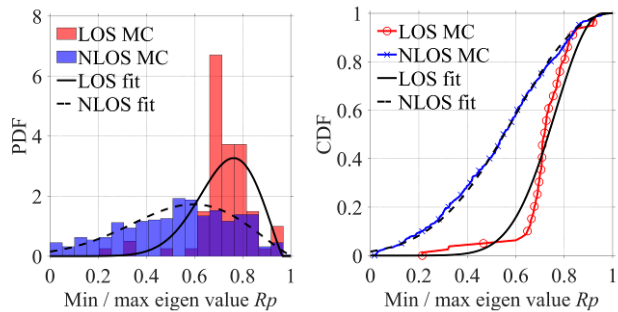


Fig 13 PDF and CDF of measured co-kurtosis eigenvalue ratios R_p

The statistical distribution of the measured time-domain kurtosis K_t and frequency-domain kurtosis K_f are presented in Fig 14. In Fig 14 (a), K_t statistics exhibit a similar behavior than in simulation (Fig 8 (a)) 90% of K_t values are smaller than 120 in NLOS clusters while it is only 4% in LOS clusters. The difference in K_f distributions in LOS and NLOS clusters is also similar to Fig 8 (b). 65% of LOS propagation CFR kurtosis is smaller than 120, which gives a large overlapping area with NLOS propagation.

The PDF and CDF of measured excess delay $\bar{\tau}$ and RMS delay spread τ_{rms} are shown in Fig 15. Both measured average excess delay and RMS delay spread of LOS propagation are not as concentrated as in simulations in Fig 9. Indeed, in measurements, LOS clusters contain usually some multipath due to possible reflections in the

³Unlike in simulations, the ratio differs from 1 as the antenna beamwidth is not identical in both angular planes.

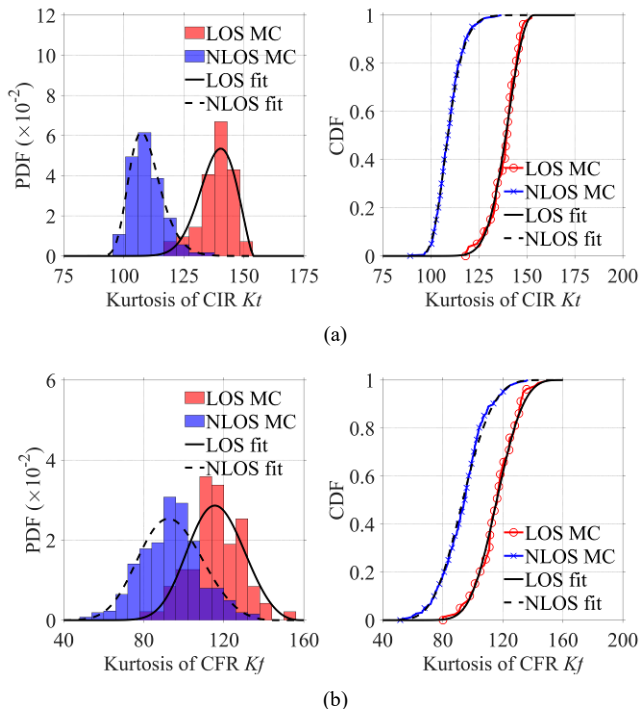


Fig 14 PDF and CDF of measured (a) time-domain kurtosis K_t and (b) frequency-domain kurtosis K_f

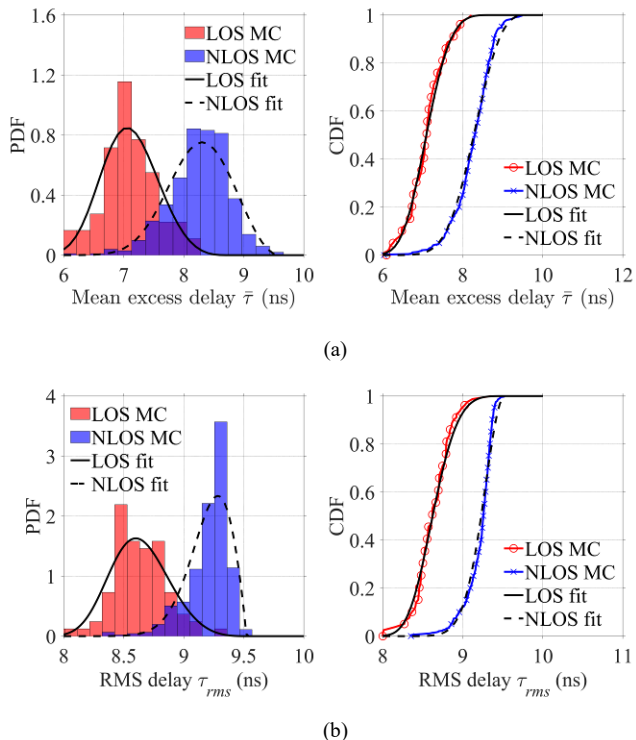


Fig 15 PDF and CDF of measured (a) mean excess delay $\bar{\tau}$ and (b) RMS delay τ_{rms} .

vicinity of the antennas. Despite this, the shapes of the LOS and NLOS PDFs for all five metrics are different from each other and suggest a possible NLOS identification.

The parameters of the GEV distributions used for fitting and the RMSE for the five statistical features are shown in Table 4. For all metrics, RMSE is lower than 0.08 in LOS and than 0.05 in NLOS.

Table 4 Measured Parameters of GEV distribution

Metrics	Parameters	LOS	NLOS
R_p	γ_p	-0.4704	-0.4474
	μ_p	0.6918	0.4712
	σ_p	0.1288	0.2400
	RMSE	0.0824	0.0103
K_t	γ_t	-0.4421	-0.0989
	μ_t	136.4	106.7
	σ_t	7.722	5.995
	RMSE	0.0267	0.0073
K_f	γ_f	-0.2298	-0.2521
	μ_f	111.3	88.11
	σ_f	13.42	15.02
	RMSE	0.0186	0.0178
$\bar{\tau}$	γ_τ	-0.2487	-0.3547
	μ_τ	6.931	8.093
	σ_τ	0.4484	0.5253
	RMSE	0.0241	0.0250
τ_{rms}	γ_{rms}	-0.2293	-0.5289
	μ_{rms}	8.541	9.167
	σ_{rms}	0.2322	0.1874
	RMSE	0.0253	0.0489

D. Performance of NLOS identification

To evaluate the performance of classification, the probabilities of type I and type II errors are shown in Table 5.

Table 5 Measured probabilities of error tested for NLOS identification

Methods	Metrics	Type I	Type II
MLR	R_p	0.1050	0.2418
	K_t	0.0200	0.0573
	K_f	0.2598	0.1228
	$\bar{\tau}$	0.1900	0.1111
	τ_{rms}	0.1750	0.1228
	$[R_p, K_t, K_f, \bar{\tau}, \tau_{rms}]$	0.1319	0.0183
ANN	$[R_p, K_t, K_f, \bar{\tau}, \tau_{rms}]$	0.0669	0.0408

Type I and II errors using MLR and all the metrics are 0.13 and 0.0183 respectively. The single metric that performs the best identification is K_t like in simulation. More metrics benefit to reduce the probability of misidentification. Type I and II errors with ANN are 0.07 and 0.04 respectively, which, unlike simulations, outperforms MLR for type I errors only. Due to weaker differences between the LOS and NLOS behavior in measurements than in simulations, identification errors are slightly larger but overall performance appears reasonable. Results obtained with ANN are in the same order as the ones obtained experimentally in the 3.1-6.3 GHz in [30] where a 0.08 type I and a 0.09 type II errors are reported.

V. CONCLUSION

Due to wideband and enhanced spatial properties (thanks to directive antennas), the millimeter band is an excellent candidate for accurate indoor localization. However, because of severe blockage effects at these frequencies, transmissions over indirect paths are necessary, thereby introducing large errors in the positioning process. To partly mitigate those errors, the nature of propagation, i.e., LOS or NLOS, over which the wireless link is established is a key indicator. This paper reports a method for LOS/NLOS identification of all clusters existing in the whole angular channel space of a

60 GHz communication using directive beam scanning antennas. Based on the beam training strategy in IEEE 802.11ad where both TX and RX antennas scan the whole angular space, a power angular spectrum is obtained at the receiver. This readily available knowledge is here used to assess the spatial behavior of five different channel metrics, namely the spatial-domain, time-domain, and frequency-domain channel power kurtosis, the mean excess delay, and the RMS delay spread. Using these metrics, a noticeable difference between LOS and NLOS clusters is observed. The maximum likelihood ratio (MLR) and artificial neural network (ANN) are operated as classifiers. Training and testing are performed at 60 GHz, in simulation, using the IEEE 802.11ad conference room channel model and in measurement, using a VNA-based experimental setup. ANN is found to outperform MLR in most situations. Type I error, being a LOS transmission identified as NLOS, is, in simulation, about 0.1 using MLR and 0.02 using ANN, and in measurements, about 0.13 using MLR and 0.07 using ANN. Type II error, being an NLOS transmission identified as LOS, is, in simulation, about 0.04 with MLR and 0.01 with ANN, and in measurements, about 0.02 using MLR and 0.04 using ANN. These relatively low error values suggest that it is possible to identify the LOS or NLOS nature of a directional transmission at mm-wave frequencies.

REFERENCES

- [1] L. Atzori, A. Iera, and G. Morabito, "The Internet of Things: A survey," *Comput. Netw.*, vol. 54, no. 15, pp. 2787-2805, Oct 28 2010.
- [2] "Release 15," 3GPP, Valbonne, France, TR 21.915 V15.0.0, 2019.
- [3] 3GPP. "Release 17." <https://www.3gpp.org/release-17> (accessed).
- [4] A. Maltsev, V. Erceg, and E. Perahia, "Channel Models for 60 GHz WLAN Systems," IEEE, 802.11-09/0334r8, 2010.
- [5] A. Maltsev, A. Puduev, and A. Gagiev, "Channel Models for IEEE 802.11ay," IEEE, 802.11-15/1150r9, 2016.
- [6] A. Maltsev, R. Maslennikov, A. Sevastyanov, A. Khoryaev, and A. Lomayev, "Experimental Investigations of 60 GHz WLAN Systems in Office Environment," *IEEE J. Sel. Areas Commun.*, vol. 27, no. 8, pp. 1488-1499, Oct 2009.
- [7] *ISO/IEC/IEEE International Standard - Information technology--Telecommunications and information exchange between systems Local and metropolitan area networks--Specific requirements Part 11: Wireless LAN Medium Access Control (MAC) and Physical Layer (PHY) Specification*, 8802-11-2012, 21 Nov. 2012.
- [8] M. Jacob, S. Priebe, R. Dickhoff, T. Kleine-Ostmann, T. Schrader, and T. Kurner, "Diffraction in mm and Sub-mm Wave Indoor Propagation Channels," *IEEE Trans. Microw. Theory Tech.*, vol. 60, no. 3, pp. 833-844, Mar 2012.
- [9] T. Mavridis, L. Petrillo, J. Sarrazin, A. Benlarbi-Delai, and P. De Doncker, "Near-Body Shadowing Analysis at 60 GHz," *IEEE Trans. Antennas Propag.*, vol. 63, no. 10, pp. 4505-4511, Oct 2015.
- [10] G. R. MacCartney, S. J. Deng, S. Sun, and T. S. Rappaport, "Millimeter-Wave Human Blockage at 73 GHz with a Simple Double Knife-Edge Diffraction Model and Extension for Directional Antennas," *IEEE VTC Veh Technol.*, 2016.
- [11] C. Slezak, V. Semkin, S. Andreev, Y. Koucheryavy, and S. Rangan, "Empirical Effects of Dynamic Human-Body Blockage in 60 GHz Communications," *IEEE Commun. Mag.*, vol. 56, no. 12, pp. 60-66, Dec 2018.
- [12] T. Y. Bai, R. Vaze, and R. W. Heath, "Analysis of Blockage Effects on Urban Cellular Networks," *IEEE Trans. Wireless Commun.*, vol. 13, no. 9, pp. 5070-5083, Sep 2014.
- [13] M. K. Samimi, T. S. Rappaport, and G. R. MacCartney, "Probabilistic Omnidirectional Path Loss Models for Millimeter-Wave Outdoor Communications," *IEEE Wireless Commun. Lett.*, vol. 4, no. 4, pp. 357-360, Aug 2015.
- [14] S. Collonge, G. Zaharia, and G. El Zein, "Influence of the Human Activity on Wide-Band Characteristics of the 60 GHz Indoor Radio Channel," *IEEE Trans. Wireless Commun.*, vol. 3, no. 6, pp. 2396-2406, Nov 2004.
- [15] K. Venugopal and R. W. Heath, "Millimeter Wave Networked Wearables in Dense Indoor Environments," *IEEE Access*, vol. 4, pp. 1205-1221, 2016.
- [16] Z. Sahinoglu, S. Gezici, and I. Güvenc, *Ultra-wideband Positioning Systems: Theoretical Limits, Ranging Algorithms, and Protocols*. Cambridge University Press, 2008.
- [17] D. Dardari, A. Conti, U. Ferner, A. Giorgetti, and M. Z. Win, "Ranging With Ultrawide Bandwidth Signals in Multipath Environments," *Proc. IEEE*, vol. 97, no. 2, pp. 404-426, Feb 2009.
- [18] C. K. Seow and S. Y. Tan, "Non-Line-of-Sight Localization in Multipath Environments," *IEEE Trans. Mob. Comput.*, vol. 7, no. 5, pp. 647-660, May 2008.
- [19] A. Jafari, T. Mavridis, L. Petrillo, J. Sarrazin, M. Peter, W. Keusgen, P. De Doncker, and A. Benlarbi-Delai, "UWB Interferometry TDOA Estimation for 60-GHz OFDM Communication Systems," *IEEE Antennas Wirel. Propag. Lett.*, vol. 15, pp. 1438-1441, 2016.
- [20] D. Dardari, P. Closas, and P. M. Djuric, "Indoor Tracking: Theory, Methods, and Technologies," *IEEE Trans. Veh. Technol.*, vol. 64, no. 4, pp. 1263-1278, Apr 2015.
- [21] A. F. Molisch, "Ultra-Wide-Band Propagation Channels," *Proc. IEEE*, vol. 97, no. 2, pp. 353-371, Feb 2009.
- [22] R. C. Qiu, "A Study of the Ultra-Wideband Wireless Propagation Channel and Optimum UWB Receiver Design," *IEEE J. Sel. Areas Commun.*, vol. 20, no. 9, pp. 1628-1637, Dec 2002.
- [23] A. F. Molisch, D. Cassioli, C. C. Chong, S. Emami, A. Fort, B. Kannan, J. Karedal, J. Kunisch, H. G. Schantz, K. Siwiak, and M. Z. Win, "A Comprehensive Standardized Model for Ultrawideband Propagation Channels," *IEEE Trans. Antennas Propag.*, vol. 54, no. 11, pp. 3151-3166, Nov 2006.
- [24] J. Khodjaev, Y. Park, and A. S. Malik, "Survey of NLOS Identification and Error Mitigation Problems in UWB-Based Positioning Algorithms for Dense Environments," *Ann Telecommun.*, vol. 65, no. 5-6, pp. 301-311, Jun 2010.
- [25] M. Pätzold, *Mobile Radio Channels*, 2nd ed. John Wiley & Sons, Ltd.
- [26] C. Tepedelenioglu, A. Abdi, and G. B. Giannakis, "The Ricean K factor: Estimation and Performance Analysis," *IEEE Trans. Wireless Commun.*, vol. 2, no. 4, pp. 799-810, Jul 2003.
- [27] L. J. Greenstein, D. G. Michelson, and V. Erceg, "Moment-Method Estimation of the Ricean K-Factor," *IEEE Commun. Lett.*, vol. 3, no. 6, pp. 175-176, Jun 1999.
- [28] J. Borras, P. Hatrack, and N. B. Mandayam, "Decision Theoretic Framework for NLOS Identification," presented at the 48th IEEE Vehicular Technology Conference, Vols 1-3, 1998
- [29] I. Guvenc, C. C. Chong, and F. Watanabe, "NLOS Identification and Mitigation for UWB Localization Systems," presented at the 2007 IEEE Wireless Communications & Networking Conference, Vols 1-9, 2007
- [30] S. Marano, W. M. Gifford, H. Wymeersch, and M. Z. Win, "NLOS Identification and Mitigation for Localization Based on UWB Experimental Data," *IEEE J. Sel. Areas Commun.*, vol. 28, no. 7, pp. 1026-1035, Sep 2010.
- [31] M. Heidari, N. A. Alsindi, and K. Pahlavan, "UDP Identification and Error Mitigation in ToA-Based Indoor Localization Systems using Neural Network Architecture," *IEEE Trans. Wireless Commun.*, vol. 8, no. 7, pp. 3597-3607, Jul 2009.
- [32] I. Guvenc and C. C. Chong, "A Survey on TOA Based Wireless Localization and NLOS Mitigation Techniques," *IEEE Commun. Surv. Tutor.*, vol. 11, no. 3, pp. 107-124, 2009.
- [33] J. Brady, N. Behdad, and A. M. Sayeed, "Beamspace MIMO for Millimeter-Wave Communications: System Architecture, Modeling, Analysis, and Measurements," *IEEE Trans. Antennas Propag.*, vol. 61, no. 7, pp. 3814-3827, Jul 2013.
- [34] X. Y. Gao, L. L. Dai, S. F. Han, I. Chih-Lin, and X. D. Wang, "Reliable Beamspace Channel Estimation for Millimeter-Wave Massive MIMO Systems with Lens Antenna Array," *IEEE Trans. Wireless Commun.*, vol. 16, no. 9, pp. 6010-6021, Sep 2017.
- [35] H. T. He, C. K. Wen, S. Jin, and G. Y. Li, "Deep Learning-Based Channel Estimation for Beamspace mmWave Massive MIMO Systems," *IEEE Wireless Commun. Lett.*, vol. 7, no. 5, pp. 852-855, Oct 2018.
- [36] W. Roh, J. Y. Seol, J. Park, B. Lee, J. Lee, Y. Kim, J. Cho, K. Cheun, and F. Aryanfar, "Millimeter-Wave Beamforming as an Enabling Technology for 5G Cellular Communications: Theoretical Feasibility and Prototype Results," *IEEE Commun. Mag.*, vol. 52, no. 2, pp. 106-113, Feb 2014.
- [37] S. Sun, T. S. Rappaport, R. W. Heath, A. Nix, and S. Rangan, "MIMO for Millimeter-Wave Wireless Communications: Beamforming, Spatial

- Multiplexing, or Both?," *IEEE Commun. Mag.*, vol. 52, no. 12, pp. 110-121, Dec 2014.
- [38] B. Q. Yang, Z. Q. Yu, J. Lan, R. Q. Zhang, J. Y. Zhou, and W. Hong, "Digital Beamforming-Based Massive MIMO Transceiver for 5G Millimeter-Wave Communications," *IEEE Trans. Microw. Theory Tech.*, vol. 66, no. 7, pp. 3403-3418, Jul 2018.
- [39] S. Kutty and D. Sen, "Beamforming for Millimeter Wave Communications: An Inclusive Survey," *IEEE Commun. Surv. Tutor.*, vol. 18, no. 2, pp. 949-973, 2016.
- [40] S. F. Han, I. Chih-Lin, Z. K. Xu, and C. Rowell, "Large-Scale Antenna Systems with Hybrid Analog and Digital Beamforming for Millimeter Wave 5G," *IEEE Commun. Mag.*, vol. 53, no. 1, pp. 186-194, Jan 2015.
- [41] J. Y. Wang, Z. Lan, C. W. Pyo, T. Baykas, C. S. Sum, M. A. Rahman, J. Gao, R. Funada, F. Kojima, H. Harada, and S. Kato, "Beam Codebook Based Beamforming Protocol for Multi-Gbps Millimeter-Wave WPAN Systems," *IEEE J. Sel. Areas Commun.*, vol. 27, no. 8, pp. 1390-1399, Oct 2009.
- [42] T. Nitsche, C. Cordeiro, A. B. Flores, E. W. Knightly, E. Perahia, and J. C. Widmer, "IEEE 802.11ad: Directional 60 GHz Communication for Multi-Gigabit-per-Second Wi-Fi," *IEEE Commun. Mag.*, vol. 52, no. 12, pp. 132-141, Dec 2014.
- [43] Y. Ghasempour, C. R. C. M. da Silva, C. Cordeiro, and E. W. Knightly, "IEEE 802.11ay: Next-Generation 60 GHz Communication for 100 Gb/s Wi-Fi," *IEEE Commun. Mag.*, vol. 55, no. 12, pp. 186-192, Dec 2017.
- [44] J. Kim and A. F. Molisch, "Fast Millimeter-Wave Beam Training with Receive Beamforming," *J Commun Netw-S Kor*, vol. 16, no. 5, pp. 512-522, Oct 2014.
- [45] D. De Donno, J. Palacios, and J. Widmer, "Millimeter-Wave Beam Training Acceleration Through Low-Complexity Hybrid Transceivers," *IEEE Trans. Wireless Commun.*, vol. 16, no. 6, pp. 3646-3660, Jun 2017.
- [46] R. M. Buehrer, H. Wymeersch, and R. M. Vaghefi, "Collaborative Sensor Network Localization: Algorithms and Practical Issues," *Proc. IEEE*, vol. 106, no. 6, pp. 1089-1114, Jun 2018.
- [47] P. Indirayanti, T. Ayhan, M. Verhelst, W. Dehaene, and P. Reynaert, "A mm-Precise 60 GHz Transmitter in 40 nm CMOS for Discrete-Carrier Indoor Localization," *IEEE J. Solid-St. Circ.*, vol. 50, no. 7, pp. 1604-1617, Jul 2015.
- [48] A. Jafari, L. Petrillo, J. Sarrazin, D. Lautru, P. De Doncker, and A. Benlarbi-Delai, "TDOA Estimation Method Using 60 GHz OFDM Spectrum," *Int J Microw Wirel T*, vol. 7, no. 1, pp. 31-35, Feb 2015.
- [49] A. Shahmansoori, G. E. Garcia, G. Destino, G. Seco-Granados, and H. Wymeersch, "Position and Orientation Estimation Through Millimeter-Wave MIMO in 5G Systems," *IEEE Trans. Wireless Commun.*, vol. 17, no. 3, pp. 1822-1835, Mar 2018.
- [50] J. W. Zhao, F. F. Gao, W. M. Jia, S. Zhang, S. Jin, and H. Lin, "Angle Domain Hybrid Precoding and Channel Tracking for Millimeter Wave Massive MIMO Systems," *IEEE Trans. Wireless Commun.*, vol. 16, no. 10, pp. 6868-6880, Oct 2017.
- [51] H. Wymeersch, G. Seco-Granados, G. Destino, D. Dardari, and F. Tufvesson, "5g Mm Wave Positioning for Vehicular Networks," *IEEE Wirel. Commun.*, vol. 24, no. 6, pp. 80-86, Dec 2017.
- [52] X. R. Cui, T. A. Gulliver, J. Li, and H. Zhang, "Vehicle Positioning Using 5G Millimeter-Wave Systems," *IEEE Access*, vol. 4, pp. 6964-6973, 2016.
- [53] X. L. Liang, Y. H. Jin, H. Zhang, and T. T. Lyu, "NLOS Identification and Machine Learning Methods for Predicting the Outcome of 60GHz Ranging System," *Chinese J Electron*, vol. 27, no. 1, pp. 175-182, Jan 2018.
- [54] X. L. Liang, H. Zhang, T. T. Lv, X. R. Cui, and T. A. Gulliver, "A Novel Scheme for NLOS Identification using Energy Detector in 60 GHz Systems," *Int J Futur Gener Co*, vol. 9, no. 6, pp. 151-164, Jun 2016.
- [55] A. Huang, L. Tian, T. Jiang, and J. Zhang, "NLOS Identification for Wideband mmWave Systems at 28 GHz," presented at the 89th IEEE Vehicular Technology Conference (VTC Spring), Kuala Lumpur, Malaysia, 28 April-1 May 2019, 2019.
- [56] B. Hu, H. Tian, and S. Fan, "Millimeter Wave LOS/NLOS Identification and Localization via Mean-Shift Clustering," presented at the IEEE 30th Annual International Symposium on Personal, Indoor and Mobile Radio Communications (PIMRC), Istanbul, Turkey, 8-11 Sept, 2019.
- [57] R. Charbonnier, C. Lai, T. Tenoux, D. Caudill, G. Gougeon, J. Senic, C. Gentile, Y. Corre, J. Chuang, and N. Golmie, "Calibration of Ray-Tracing With Diffuse Scattering Against 28-GHz Directional Urban Channel Measurements," *IEEE Trans. Veh. Technol.*, vol. 69, no. 12, pp. 14264-14276, Dec 2020.
- [58] P. Lyu, A. Benlarbi-Delai, Z. Ren, and J. Sarrazin, "Spatially Clustering with Watershed Transformation for Millimeter Wave Indoor Channel Modeling," *arXiv:2009.01375*, 2020.
- [59] N. Czink, P. Cera, J. Salo, E. Bonek, J. P. Nuutinen, and J. Ylitalo, "A Framework for Automatic Clustering of Parametric MIMO Channel Data Including Path Powers," presented at the 2006 IEEE 64th Vehicular Technology Conference, 2006.
- [60] B. Efron and R. J. Tibshirani, *An Introduction to the Bootstrap*. Chapman and Hall/CRC, 1993, p. 456.